Effect of DM Actuator Errors on the WFIRST/AFTA Coronagraph Contrast Performance

***Erkin Sidick and Fang Shi**
Jet Propulsion Laboratory, California Institute of Technology, 4800 Oak Grove Drive, Pasadena, CA 91109, USA

ABSTRACT

The WFIRST/AFTA 2.4 m space telescope currently under study includes a stellar coronagraph for the imaging and the spectral characterization of extrasolar planets. The coronagraph employs two sequential deformable mirrors (DMs) to compensate for phase and amplitude errors in creating dark holes. DMs are critical elements in high contrast coronagraphs, requiring precision and stability measured in picometers to enable detection of Earth-like exoplanets. Working with a low-order wavefront-sensor the DM that is conjugate to a pupil can also be used to correct low-order wavefront drift during a scientific observation. However, not all actuators in a DM have the same gain. When using such a DM in low-order wavefront sensing and control subsystem, the actuator gain calibration errors introduce high-spatial frequency errors to the DM surface and thus worsen the contrast performance of the coronagraph. We have investigated the effects of actuator gain calibration errors and the actuator command digitization errors on the contrast performance of the coronagraph through modeling and simulations, and will present our results in this paper.

Key words: Coronagraphy, adaptive optics, space telescopes, exoplanets

1. INTRODUCTION

NASA's Science Mission Directorate has begun the study phase of the WFIRST-AFTA mission [1], with an anticipated launch date early in the next decade. That study included a high-contrast stellar coronagraph to complement the WFIRST instrument. There are currently three coronagraph technologies being developed/considered for the WFIRST-AFTA coronagraph [2]. They are a Hybrid Lyot Coronagraph (HLC) [3-4], a Phase-Induced Amplitude Apodization Complex Mask Coronagraph (PIAACMC) [5], and a Shaped-Pupil Coronagraph [6]. These technologies have the ability to produce high contrast at a small working angle even in the presence of the WFIRST-AFTA's obscured pupil. However, one of the challenges faced by the WFIRST-AFTA coronagraphic telescope is the optical wavefront stability necessary to achieve the required level of starlight suppression. The wavefront dynamics faced by the coronagraph can be decomposed into several components, and one of them is the low-order wavefront (LOWF) drift at frequencies below 2Hz [7-8]. It is largely caused by the sunshine and the Earth shine driven thermal changes in the telescope optics and the telescope structure. The current approach being pursued to mitigate the impact of the LOWF drift is to measure and suppress the LOWF errors presented to the coronagraph in order to reduce them and keep them in an acceptable level. This is being done in a WFRIST-AFTA Low-Order Wavefront Sensing and Control (LOWFS/C) subsystem [7-8]. It consists of a low-order wavefront-sensor (LOWFS) and a DM, i.e., DM1, which is conjugate to a pupil. However, not all actuators in a DM have the same gain [9]. When using such a DM in a LOWFS/C subsystem, the actuator gain calibration errors introduce high-spatial frequency errors to the DM surface and thus worsen the contrast performance of the coronagraph. Also, actuator command digitization errors bring about a mismatch between the actuator commands needed and those actually applied. We have investigated the effects of DM actuator gain calibration errors and actuator command digitization errors on the contrast performance of a coronagraph through modeling and simulations, and will present our results in this paper. Specific case considered in this paper as an example includes low-order wavefront control (LOWFC) process in an HLC.

2. BACKGROUND

In this paper, we investigate the impact of the actuator gain errors as well as the actuator command digitization errors on

*Erkin.Sidick@jpl.nasa.gov; Phone 1 818 393-7585; Fax 1 818 393-3290; www.jpl.nasa.gov

Techniques and Instrumentation for Detection of Exoplanets VII, edited by Stuart Shaklan, Proc. of SPIE Vol. 9605
960506 · © 2015 SPIE · CCC code: 0277-786X/15/$18 · doi: 10.1117/12.2188240

the LOWFC process in an HLC configuration. An overview of the above-mentioned three coronagraph configurations is provided in Refs. [4, 10]. Therefore, we do not provide a detailed description of the HLC in this paper. Instead, we present some brief background information related to LOWFC in HLC. That information is useful for the better understanding of the impact of actuator gain errors and actuator command digitization errors on the LOWFC efficiency as well as on the broadband contrast of HLC. All the simulation results to be presented below were obtained for an optical system where the beam diameter on DM1 is 2mm smaller than the width of DM1 active area.

2.1 Nominal Contrast of HLC

Figure 1(a) shows the AFTA telescope obscuration pattern. In the PROPER simulation tool of HLC being used in the current studies [4], this pattern is used as the primary mirror clear-aperture. The HLC [11] is a modification of the classical Lyot coronagraph that consists of an occulting mask located at an intermediate focal plane and a pupil mask (Lyot stop) at a subsequent pupil plane. In the HLC the focal plane mask (FPM) is a combination of patterned amplitude and phase modulating coatings. Both are simultaneously optimized to provide an acceptable compromise in inner-working angle (IWA), contrast, bandwidth, and throughput, with the wavelength-dependent characteristics of the materials included. Like most coronagraphic techniques the performance of the HLC is seriously degraded by obscurations in the telescope. As part of the design optimization process the DMs were used to alter the wavefront to reduce the diffractive effects of these obscurations, resulting in a complicated pattern of actuator settings with relatively large strokes. The DM patterns are an inherent part of diffraction control and would be used whether there are

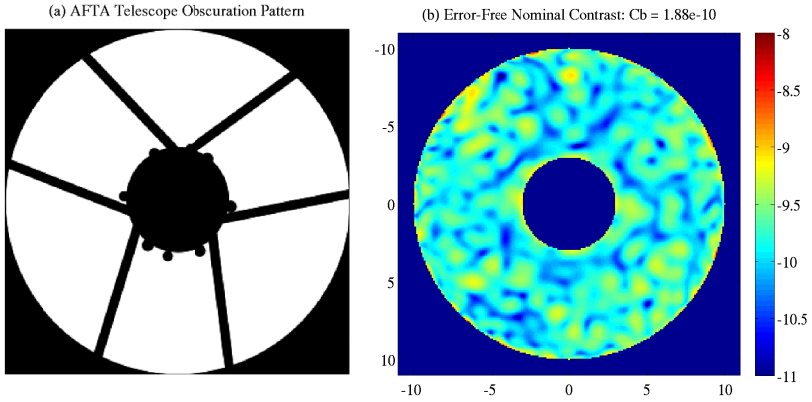

Figure 1. (a) The AFTA telescope obscuration pattern. It is the "old" pattern and includes metrology markers along the edge of the secondary obscuration. Because the primary and the secondary mirrors will be refigured and recoated, these will be removed. The HLC design simulated here is for this "old" pattern. (b) Contrast map of the aberration-free HLC obtained with the default DM1 and DM2 actuator solutions. The *x*- and *y*-axes are field angle in λ/D.

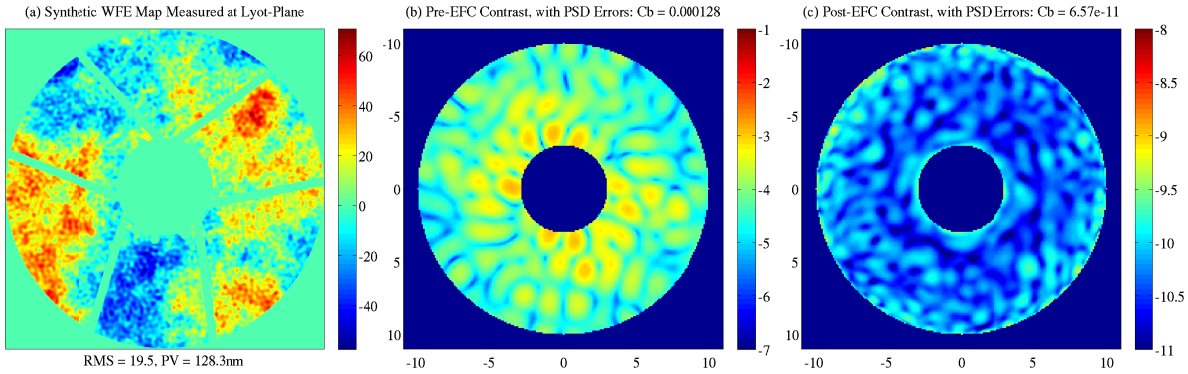

Figure 2. (a) Synthetic phase error maps generated using a PSD specification that is used in the simulations to represent optical surface fabrication errors. Each optic has a different pair of amplitude and phase PSD error maps and WFE map in part (b) includes the phase errors of all the optics up to Lyot-Stop. Given in the x-label are the root-mean-square (RMS) and peak-to-valley (PV) values of the WFE map. (b) Pre-EFC contrast map of the aberrated HLC. (c) Contrast map of the aberrated HLC obtained after 20 EFC iterations. It is referred to as "nominal contrast" in this paper. The *x*- and *y*-axes in parts (b-c) are field angles in λ/D.

aberrations in the system or not. The HLC configuration used here was designed by Dwight Moody and John Trauger at NASA's Jet Propulsion Laboratory (JPL) to have an IWA of 4 λ/D and an outer working-angle (OWA) of 13.5 λ/D at λ = 550 nm. The occulter and DM patterns were optimized to provide good contrast in the 523 – 578nm wavelength range and reduced sensitivity to pointing errors assuming a 1.6 mas RMS jitter [4], when there is no other error in the optical system except AFTA obscurations and jitter.

Typically at least nine wavelengths are used in the occulter and DM stroke optimization and subsequent performance simulations. But we use four wavelengths, namely, 0.529375, 0.543125, 0.556875, and 0.57062μm, to save computation time in this paper. This is acceptable because we are only interested in the relative performance of the HLC here. We refer to a system as "aberration-free" when there is no other error except AFTA obscurations, and we do not include any jitter error in this paper.

The aberration-free, design HLC yields a contrast map as shown in Fig. 1(b). For the current optical system with two DMs, we evaluate the contrast over a region Ω_b, where Ω_b is annular-shaped dark-hole region bound by $3\lambda/D \le R \le 10\lambda/D$, with $X = x/f$, $Y = y/f$, $R = \sqrt{X^2 + Y^2}$, x and y are the horizontal and the vertical position variables on the corresponding image-plane, and f is the focal length. The contrast is equal to the image intensity of the occulted star divided by the maximum values of the un-occulted, field-dependent star intensity [4, 10]. The C_b given in the title of Fig. 1(b) is the mean value of the contrast inside the dark-hole area.

In our current studies we work with a realistic, aberrated system by creating synthetic phase and amplitude error maps for each optic from PSDs representative of those of similar real optics, and including them in the HLC model [10]. Figure 2(a) shows the WFE at the Lyot-plane of this aberrated system. It includes the phase errors of all the optics up to Lyot-Stop. After introducing such phase and amplitude errors, the contrast map of the HLC degrades to that of Fig. 2(b). By carrying-out additional WFC for about 20 iterations using the method called "Electric Field Conjugation" (EFC) [12], we obtain a new contrast map as shown in Fig. 2(c). The dark-hole of Fig. 2(c) was generated with two sequential DMs positioned one meter apart to provide both phase and amplitude control over a 360º field around the star. Each of them has 48x48 actuators. We call the contrast map in Fig. 2(c) the "nominal contrast", and the corresponding optical system as the "nominal HLC". We will introduce additional LOWFE to this nominal HLC in the later sections of the paper. It should be noted that the C_b-value of Fig. 2(c) is better than that of Fig. 1(b) not because the EFC did a better job in the latter, but because two different sets of wavelengths were used in those two optimization processes.

2.2 Contrast Sensitivity to Zernike-Mode Aberrations

During the coronagraph observation, the thermal load variation from the Sun and the Earth due to the spacecraft orbiting or telescope pointing will cause the surface figures and the positions of the telescope optics to change. This will give rise to some amount of low-order wavefront error (WFE). Figures 3(a-b) show the model-predicted thermally-induced WFE for a notional coronagraph Observation Scenario 3 (OS3) with the Earth present corresponding to a time-span of 56 hours (Refs. [8, 10] show a newer version of OS3 thermal drift data, the one without the Earth present). We can see from these plots that the dominant components of the WFE are focus, astigmatism and coma generated by the thermally induced position shifts of the telescope optics. Higher aberration modes beyond spherical are all negligibly small, in single-digit picometers. It is also evident that the wavefront drift is very slow compared to Line-of-Sight (LoS) jitter [8], typically under 0.001 Hz. For most optical systems wavefront drift less than 0.5 nm RMS is insignificant. However, the broadband contrast performance of a high-contrast coronagraph is very sensitive to wavefront drifts. The science requires the WFIRST coronagraph to have raw, broadband contrast better than 10^{-8}. Furthermore, in order to differentiate planets from residual speckles inside the dark-hole area and detect a planet with proper signal-to-noise ratio, the coronagraph contrast needs to be stable at a level of ~ 10^{-10} during the observation. This stability requirement drives a very tight tolerance for the wavefront drift.

Figures 4(a-b) show the contrast sensitivities of an HLC to various low-order Zernike-mode aberrations with a coefficient of 10 and 20pm (picometers), respectively. Here 10 and 20pm RMS of individual aberrations are separately injected into the HLC system and propagated to create new point-spread function (PSF) images. The root-mean-square (RMS) values of the difference between the before- and the after-aberration maps is plotted versus field-angle radius to indicate which aberrations are of primary concern. We can see from these plots that the coronagraph contrast sensitivity depends on the mode of Zernike aberrations, with spherical, coma, and trefoil being the worst offenders. As is shown in Ref. [8], the coronagraph contrast sensitivity also depends on the instrument operating modes of Occulting Mask Coronagraph (OMC), i.e., HLC, PIAACMC and SPC. In this paper, we investigate the impact of the actuator gain errors

as well as the actuator command digitization errors in an HLC configuration. Therefore, we did not include the contrast sensitivity plots for the other two configurations here. We can see from the WFIRST-AFTA thermal drift (Fig. 3) and these coronagraph contrast sensitivities that the thermally-induced WFE drift needs to be sensed and corrected in order to achieve the coronagraph stability requirement.

In general, the coronagraph contrast scales with WFE squared. That means that the most sensitive modes, such as spherical, coma, and trefoil, need to be stable at a few tens of picometers in order to maintain the contrast stability at ~10^{-10} level, as we can see from Fig. 4. These are the wavefront changes that must be measured and corrected by the LOWFS/C subsystem. The LOWFS/C subsystem of the WFIRST coronagraph works with the coronagraph's high-order wavefront sensing and control (HOWS/C) subsystem, which is responsible for generating the coronagraph's dark-hole using the coronagraph's two DMs [10]. The LOWFS/C does not set the wavefront; instead, it only maintains the wavefront set by HOWS/C. In other words, the LOWFS/C is a relative sensing and control system. Based on the coronagraph performance requirements, the LOWFS/C's sensor is designed to have LoS sensitivity of 0.4 milli-arcsec and LOWF – focus (Z_4) to spherical (Z_{11}) – sensitivity on the order of 10 pm.

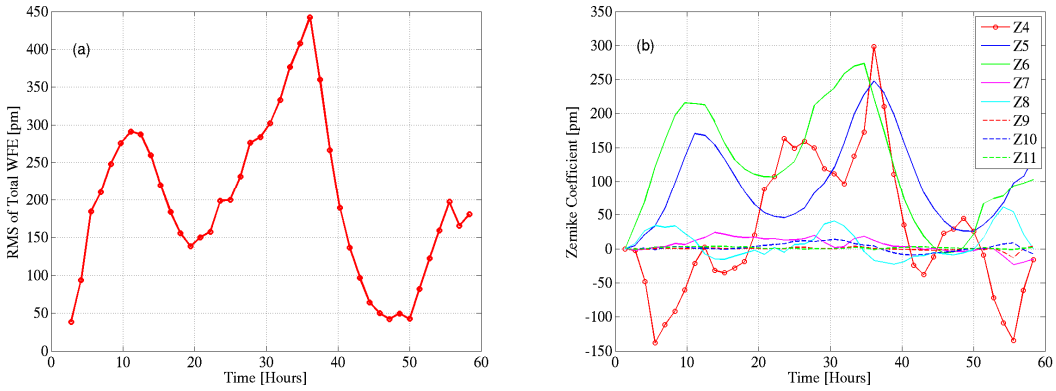

Figure 3. Thermal drift WFE of the WFIRST-AFTA from a typical coronagraph observation scenario. (a) Total WFE. (b) Low-order Zernike-mode components (Z_4 – Z_{11}) decomposed from the total WFE drift.

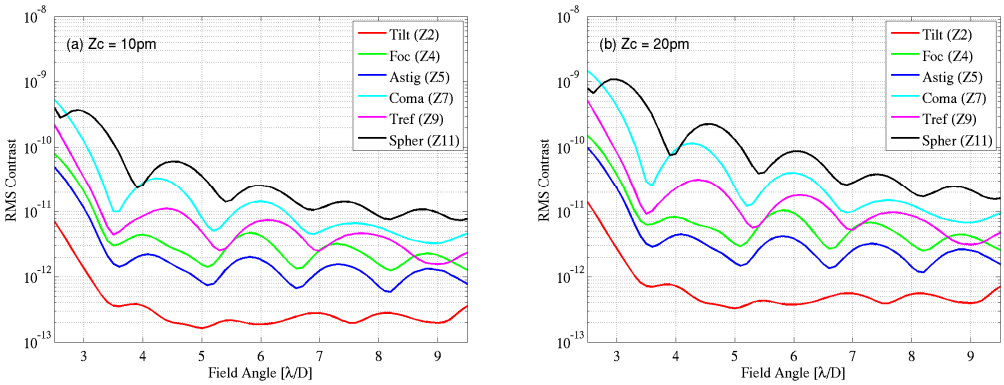

Figure 4. HLC contrast sensitivity to different Zernike aberration modes. Each curve shows the RMS values of change in 10% broadband contrast as a function of field-angle. (a) The coefficient of each Zernike aberration mode, Z_c, is equal to 10pm. (b) Z_c = 20pm.

3. ACTUATOR GAIN CALIBRATION ERRORS

In this section we investigate the effects of actuator gain errors on the efficiency of low-order wavefront control (LOWFC). As mentioned above, HLC will include a LOWFS/C system to maintain wavefront stability over time. In the HLC the FPM or occulter is reflective and directs the rejected stellar PSF core into a Zernike phase contrast sensor [8, 13]. A patterned phase modulating coating on the FPM causes internal interference that transforms phase errors into measureable intensity variations when the reflected beam is imaged onto a detector at a pupil. A LOWFS model has

been developed and implemented into our simulation tool [8], and we use that model in this paper. Each LOWFS/C step includes the sensing the change in LOWF with the LOWFS subsystem (described above) first, calculating an update for control commands according to the change in LOWF next, and finally applying the changes in control commands to appropriate control optics. That is, although the WFC to reduce scattered light and generate a dark hole around the star is carried out with two DMs, the LOWFC is done with only one DM, namely, DM1. Also, the tip/tilt control is accomplished by adjusting the tilting angle of a fast-steering mirror (FSM), and the focus adjustment is made through a flat-mirror (FM).

In general, one can expect that the actuator height (h) versus actuator voltage (V) curve of each actuator is nonlinear and these curves are different for different actuators. Some preliminary measurements of the actuator response curves for an older version of the DM have indeed exhibited the evidence of such behavior, as is shown in Figs. 9(a-b) of Ref. [9]. Based on the knowledge learned from those measurements, a model of actuator nonlinear response curves with some random slope errors was proposed. It is expressed as

$$h_i(V_i, \delta_i) = (1 + \delta_i) h(V_i), \qquad -50 \le h_i \le 50\text{V} \tag{1}$$

where $h(V_i)$ is a 5th-order polynomial function of V_i, and index i indicates the actuator number. In Ref. [9], δ_i were treated as normally-distributed random numbers obtained from the Matlab function *randn.m* and re-scaled the negative and positive parts separately such that $-0.3 \le \delta_i \le +0.3$. It was claimed in Ref. [9] that this range of the δ_i values roughly corresponds to the dh/dV data in Fig. 9(b) of Ref. [9] at $V = 30$V (for the 0 – 100V voltage range). That is, it was shown that the older version of the DM exhibited up to ±30% actuator gain non-uniformity.

The uniformity of the actuator gains can be expected to have been improved since the measurement reported in Ref. [9] was made, and the characterization of the actuator gain distribution of the current DM's is currently underway at JPL. However, in general we can expect that the actuator gain calibration errors always exist. In what follows, we consider uniformly distributed random actuator gain calibration errors of up to ±20%.

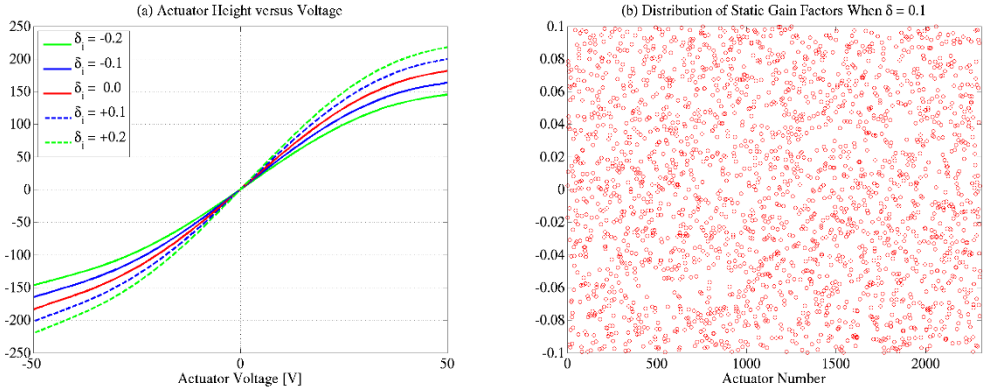

Figure 5. (a) Several examples of actuator response curves obtained from Eqn. (1). (b) Distribution of static actuator gain error factors, $\{\delta_i\} = r(\delta)$, when $\delta = 0.1$. The variable i indicates the actuator number. The values of $r(\delta)$ presented in this plot are used in the current studies. It has a uniform distribution in the $[-\delta, \delta]$ range.

Figure 5(a) shows five examples of actuator responsive curves obtained from Eqn. (1). In general, the range of actuator strokes required in LOWFC is about 1nm or less. Therefore, we ignore the nonlinearity of the actuator response and treat $h(V_i)$ as a linear-function of V_i, that is, $h_i = h(V_i) = 5V_i \times (\text{nm/V})$. On the HCIT testbed, actuator commands take a value in the 0 – 100V range, and the corresponding actuator heights take a value in the 0 – 500nm range. But in our simulations we use [-50, +50] V for the actuator commands and [-250, +250] nm for the actuator heights for convenience.

We take into account the static and the dynamic actuator gain errors affecting the LOWF maintenance process in the following form:

$$h(V_i, \delta_i, t_j) = h(V_i, \delta_i, t_{j-1}) + H(V_i, t_j) \times [1 + r(\delta)] \times [1 + r(\gamma, t_j)], \tag{2}$$

where $h(V_i, \delta_i, t_{j-1})$ are the actuator heights in the previous or the (j-1)th time-step, $\{\delta_i\} = r(\delta)$ are the random actuator static gain errors having a uniform distribution as shown in Fig. 5(b) for $\delta = 0.1$ as an example, $\{\gamma_i\} = r(\gamma, t_j)$ are the random actuator dynamic gain errors, and $H(V_i, t_j)$ are the actuator height updates corresponding to the current time-step. The values of $H(V_i, t_j)$ are determined by the control algorithm based on the change in LOWF. The $r(\gamma, t_j)$ also has a uniform distribution in the [-γ, γ] range. In this study, we always use $\gamma = \delta/2$ without explicitly mentioning the value of γ. Note that the values and the distribution of $\{\gamma_i\} = r(\gamma, t_j)$ change in every time-step even if the value of γ is kept the same.

We investigate the effects of actuator gain errors on the LOWFC efficiency by estimating and controlling the $Z_2 - Z_{11}$ components of the OS3 thermal drift in Figs. 3a-(b). ($Z_2 - Z_3$ components are not shown explicitly in these plots). We carry out the $Z_2 - Z_{11}$ estimation with a Zernike wavefront sensor (ZWFS) model described in Ref. [8]. It is based on the known physical parameters of a 16x16 array sensor used on our testbed. On the testbed, the $Z_2 - Z_3$ (tip/tilt) components are controlled with a fast-steering mirror (FSM), the Z_4 with a focus-adjusting flat-mirror (FM), and the $Z_5 - Z_{11}$ with DM1, as mentioned earlier. In the simulations we assume perfect control of $Z_2 - Z_3$. The Z_4 (focus) can be controlled to a high-degree as well, but that process generates some small amount of parasitic $Z_2 - Z_3$ and $Z_5 - Z_{11}$ errors. These parasitic errors as well as the sensing errors were all taken into account in our simulations.

The RMS of the total WFE consisting of $Z_2 - Z_{36}$ components is shown with a red-curve in Fig. 6(a). Its maximum is 443pm, and the maximum of the Z5 – Z11 components together is 337pm. Starting from the second time-step, the FSM, the FM and the DM1 actuator commands set in the previous time-step will partially correct the raw, or input, $Z_2 - Z_{11}$ errors. As a result, every data point on the red-curve changes to a data point in the blue-curve in Fig. 6(a) at the same time-step. The $Z_2 - Z_{11}$ components of the data point on the blue-curve are fed into the LOWFS. We use the $Z_5 - Z_{11}$ component of the sensor output at that time-step as an input to the LOWFC algorithm, and come up with an incremental DM1 actuator commands or a DM1 command update. After we apply this DM1 actuator height update, remove the $Z_2 - Z_4$ components from the sensor output, and calculate the total residual errors, the data point on the blue-curve changes to a point on the green-curve at the same time step. And that data point corresponds to the post-LOWFC or residual wavefront error. The blue- and the green-curves in Fig. 6(a) correspond to $\delta = 0$, and the black-curve to $\delta = 0.2$. Although the residual WFE becomes worse with increased δ–value at some time intervals, the absolute value of the residual WFE remains to be reasonably small, with its maximum being 32pm RMS when $\delta = 0.2$ in Fig. 6(a). The LOWFC process is quite effective when $\delta \leq 0.05$, and yields a post-LOWFC maximum of 19pm RMS when $\delta = 0.05$, including uncontrolled $Z_{12} - Z_{36}$ errors and focus-control parasitic errors. Figure 6(b) shows the C_b-values as a function of time. In this scenario, the mean broadband contrast can be kept below 10^{-10} level at most of the time as far as the $\delta \leq 0.1$ is guaranteed. When $\delta = 0.2$, the C_b values of the post-LOWFC contrast maps become comparable to that of

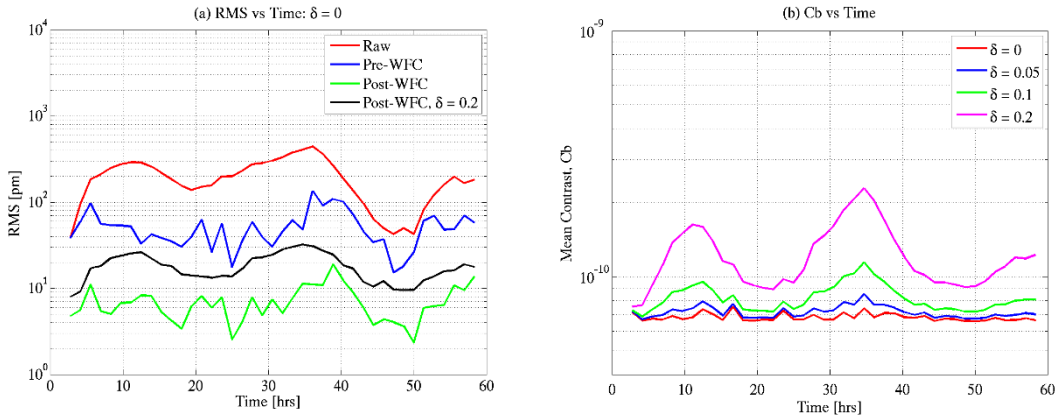

Figure 6. (a) Time dependence of the raw input LOWF used in this study, as well as the pre- (Pre-WFC) and the post-LOWFC-update (Post-WFC) wavefront errors. The red-curve consists all of the $Z_2 - Z_{36}$ components in Fig. 3(b). The blue- and the green-curves were obtained with $\delta = 0$. The black-curve (Post-WFC) corresponds to $\delta = 0.2$ and is included here as a comparison to the green-curve. (b) Mean contrast, C_b, versus time with the actuator gain error factor, δ, as a parameter.

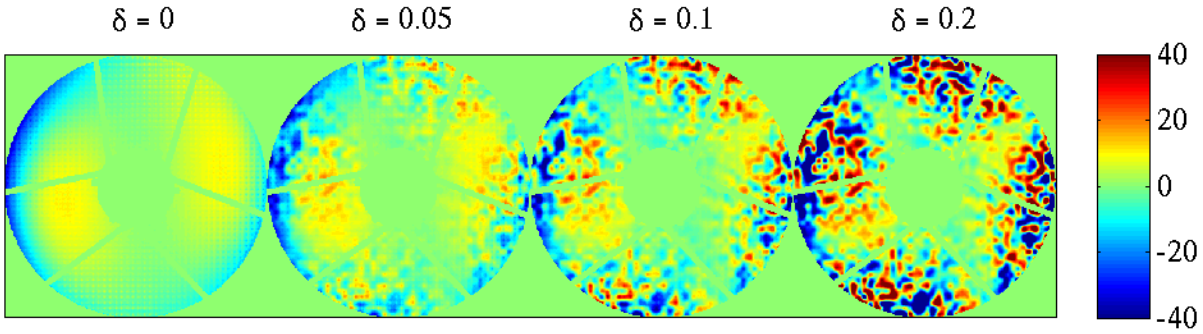

Figure 7. Post-WFC residual OPD maps at Time = 30.6hr corresponding to four different δ – values. The color-bar stretch was shortened from their natural limits to make more details of the OPD maps visible.

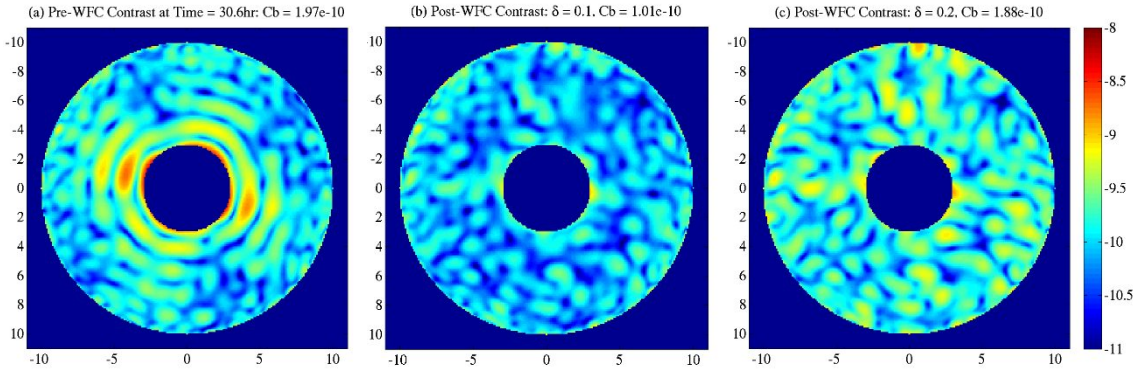

Figure 8. (a) Pre-LOWFC contrast map. (b-c) Post-LOWFC contrast maps obtained with δ = 0.1 and 0.2, respectively. All three parts correspond to a time step of Time = 30.6hr. The *x*- and *y*-axes are field angles in λ/D.

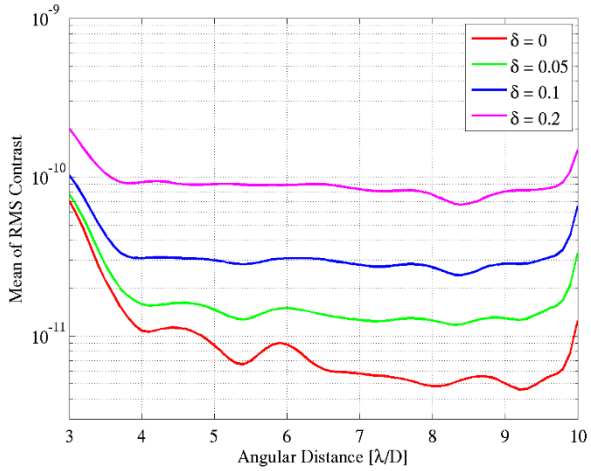

Figure 9. RMS contrast averaged across the whole time-span. Each differential contrast map is equal to a contrast map at a time-step minus the nominal. The individual RMS change computed over azimuth was obtained first, then averaged over all of the time steps. Finally it is plotted versus field radius.

the pre-LOWFC ones at most of the time (Fig. 6b), however, their radially-averaged values are quite different, as will be shown shortly.

Figure 7 shows the post-LOWFC residual OPD maps obtained at Time = 30.6hr. The impact of the actuator gain errors on the residual OPD is clearly evident in this plot. One can guess from the residual OPD maps in this plot and the contrast sensitivities in Fig. 4 that the residual WFE left over from the LOWFC does not change the HLC contrast too much. Such an expectation is confirmed by the results in Figs. 8(a-c), where part (a) shows an example of the pre-

LOWFC contrast map at Time = 30.6hr, and the remaining two parts show the post-LOWFC contrast maps obtained with δ = 0.1 and 0.2 at the same time step. Figure 9 shows the mean values of the RMS contrast curves corresponding to four different [δ, γ] pairs. To calculate these plots, the individual RMS change computed over azimuth was obtained first, then they were averaged over all of the time steps. As is seen from this plot, the contribution of the residual LOWF to contrast is well below the desired ~10^{-10} level inside the $R = 3 - 10\lambda/D$ dark-hole area when δ = 0.1 or smaller, but when δ=0.2 the RMS contrast goes up beyond the above level near the inner-working angle.

4. ACTUATOR COMMAND DIGITIZATION ERRORS

Choosing a right analog-to-digital converter (ADC) for DMs is important in guaranteeing the effectiveness of the LOWFS/C subsystem. As the second topic in our investigation, we examined the effects of actuator command digitization (or quantization) errors on the efficiency of the LOWFC in HLC. We considered three types of ADCs for DM1, and their digitization steps (or LSBs) are summarized in Table 1.

Table 1. Summary of digitization steps or LSBs for three types of A/D converters.

ADC Resolution	Digitization Step [mV]	Digitization Step [pm]
16-Bit	1.53	7.63
15-Bit	3.05	15.3
14-Bit	6.10	30.5

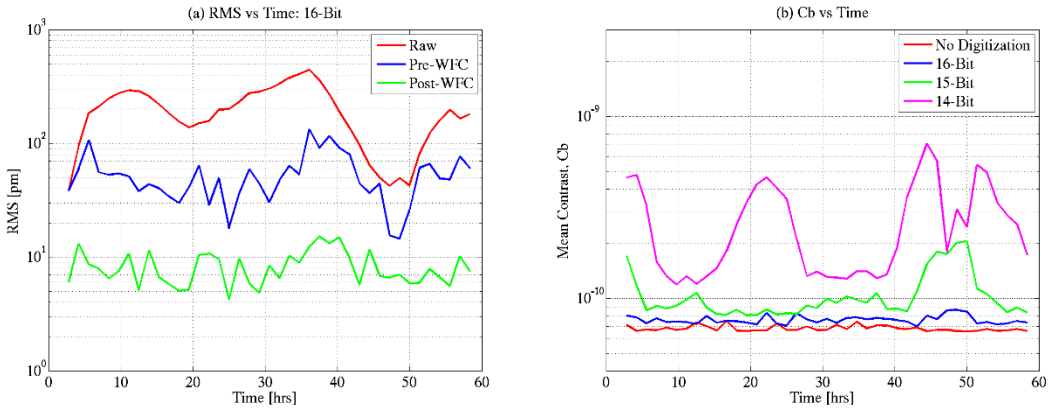

Figure 10. Same plots as Fig. 6(a), except that this plot was obtained by taking into account the actuator command digitization errors corresponding to an ADC resolution of 16-Bit. (b) Mean contrast, C_b, versus time with the ADC resolution as a parameter.

Digitization of actuator commands is implemented in the following way:

$$h(V_i, \Delta h, t_j) = \Delta h \times \text{Round}\{[h(V_i, \Delta h, t_{j-1}) + H(V_i, t_j)]/\Delta h\}, \quad (3)$$

where Δh is the digitization step in picometers given in Table 1, and "Round" is a rounding-operator that converts a real-number to the nearest integer.

We investigate the effects of actuator command digitization errors on the LOWFC efficiency by introducing the same OS3 model thermal drift WFE used in Section 3. We include the sensing and the focus-control parasitic errors in the simulations, in the same way as it was done in Section 3. The three curves in Fig. 10(a) show the input (Raw), Pre-WFC and Post-WFC wavefront error RMS values. This plot corresponds to an ADC resolution value of 16-Bit. It is noted that the post-LOWFC residual WFE can be maintained below 20pm (RMS) level with a 16-Bit. Figure 10(b) shows the mean contrast values, C_b, as a function of time for four different cases of actuator command digitization errors. As is seen from this plot, the C_b–value stays below 1x10^{-10} level when the ACD resolution is 16-Bit, and becomes much worse at some time intervals with the other two ACD resolutions.

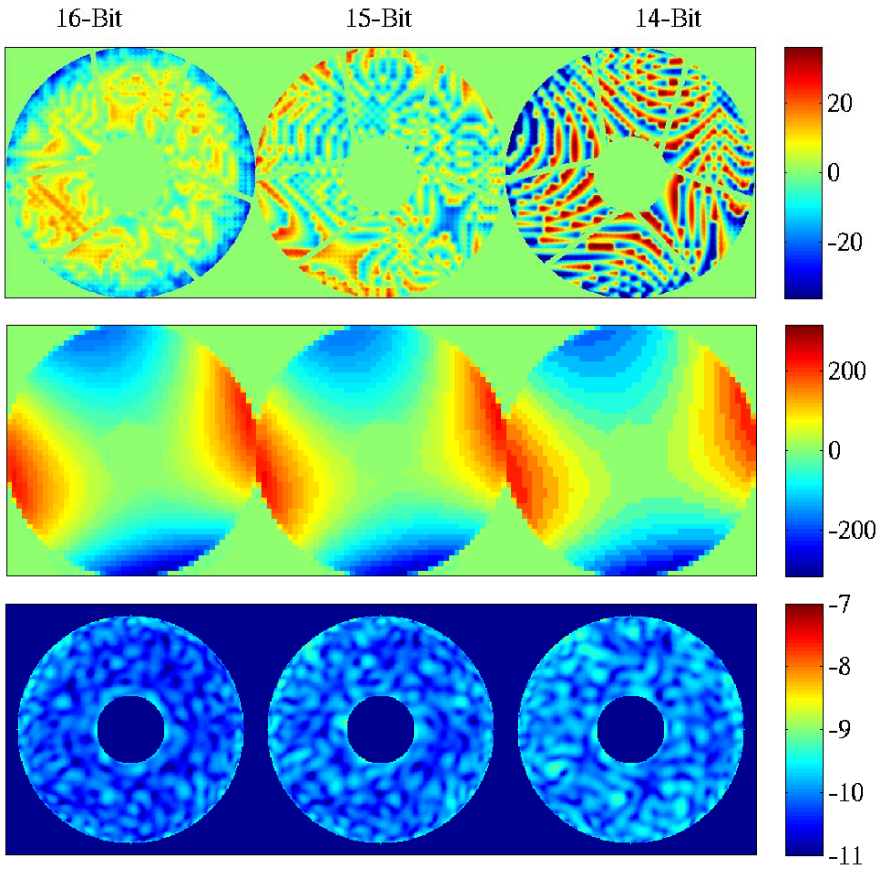

Figure 11. After LOWFC residual OPDs (top), DM1 actuator heights (middle), and post-LOWFC contrast maps (bottom) at Time = 30.6hr. The three maps in each part correspond to different ADC resolutions of 16-Bit (left), 15-Bit (middle), and 14-Bit (right), respectively.

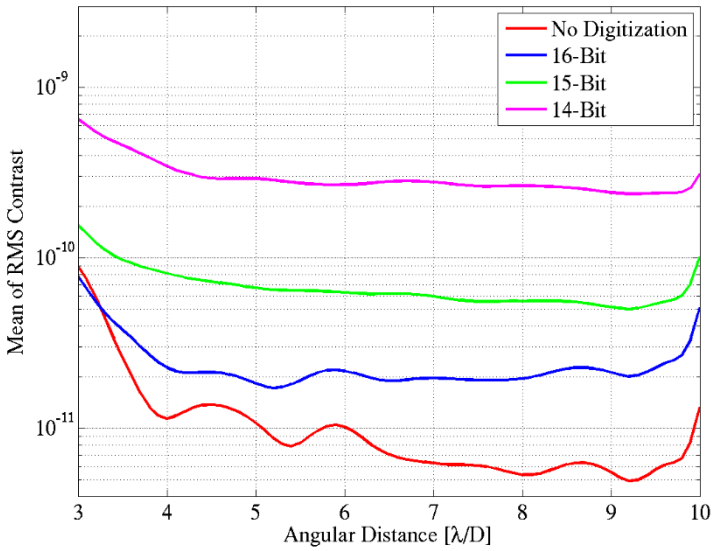

Figure 12. RMS contrast averaged across the whole time-span. Each differential contrast map is equal to a contrast map at a time-step minus the nominal. The individual RMS change computed over azimuth was obtained first, then averaged over all of the time steps. Finally it is plotted versus field radius.

A set of examples of the post-WFC residual OPDs, the DM1 actuator heights and the post-LOWFC contrast maps are shown in Fig. 11. They all correspond to the data points in Fig. 10 at Time = 30.6hr, and the three maps in each figure correspond to three different ADC resolutions of 16-Bit (left), 15-Bit (middle), and 14-Bit (right), respectively. The time-average of the RMS contrast values corresponding to four different actuator command digitization error cases are shown in Fig. 12. In this plot, the curve labeled as "No Digitization" corresponds to the digitization-error free contrast. These results show that the ADC used for DM1 must have a resolution of at least 16-Bit to keep the LOWF drift induced contrast level at $1x10^{-10}$.

5. CONCLUSION

We have investigated the effects of DM actuator gain calibration errors and actuator command digitization errors on the contrast performance of a coronagraph through modeling and simulations. In our simulations we considered a specific AFTA coronagraph configuration, that is, an HLC utilizing two DMs, as an example. We used a set of time-dependent WFE as our low-order wavefront error input and evaluated the impact of after low-order wavefront control residual WFE on the 10% broadband contrast of the coronagraph. We have shown that a DM1-based LOWFC subsystem can correct low-order WFE more than 350pm RMS to an acceptable level even when the DM actuators have uniformly-distributed random gain calibration errors as much as ±10%. We have also investigated the impact of the actuator command digitization errors on the broadband contrast. Based on our findings about the impact of the resolution of an ACD used with DM1 on the LOWFC efficiency, we have shown that the ACD must have a resolution of at least 16-Bit to maintain the broadband contrast at $1x10^{-10}$ level during the LOWFS/C operation if the thermally induced LOWF errors stay comparable to those analyzed in this paper.

Currently a testbed is being built at JPL to simulate the WFIRST-AFTA telescope LoS jitter and wavefront drift, and perform stand-alone testing of the LOWFS/C subsystem before integrating it with the coronagraph. Our early lab results using an HLC focal plane mask have shown that a Zernike wavefront sensor (ZWFS) is capable of detecting sub milli-arcsecond tilt, as needed for WFIRST coronagraph to meet its science requirements. The obtained ZWFS images closely match the model predictions, and is currently limited by the uncertainty of lab seeing.

The performances of actuators having linear responses to the command voltage but with slightly different slopes in the four-probe electric-field estimation and the EFC-based WFC operations were investigated in connection with the High Contrast Imaging Testbed Phase Induced Amplitude Apodization (HCIT/PIAA) coronagraph system at JPL, and the results were reported in Ref. [9]. It was shown that when the actuators have random, normally-distributed gain calibration errors with a standard-deviation (STD) value of up 10%, the convergence of the EFC process takes slightly longer time than normal as expected, but the achievable final contrast floor does not change much. The question of what is the distribution of the actuator gain errors in the current DMs, as well as how they affect the efficiency of EFC-based WFC operations in HLC and other two coronagraph configurations remain unexplored.

The research was carried out at the Jet Propulsion Laboratory, California Institute of Technology, under a contract with the National Aeronautics and Space Administration.

REFERENCES

[1] D. Spergel *et al*, Wide-Field Infrared Survey Telescope-Astrophysics Focused Telescope Assets WFIRST-AFTA Final Report, http://wfirst.gsfc.nasa.gov/science/sdt_public/WFIRST-AFTA_SDT_Final_Report_Rev1_130523.pdf (2013).
[2] Ilya Poberezhskiy *et al*, "Technology development towards WFIRST-AFTA coronagraph," Proc. SPIE 9143, 91430P (2014).
[3] John Trauger, Dwight Moody, Brian Gordon, "Complex apodized Lyot coronagraph for exoplanet imaging with partially obscured telescope apertures," Proc. SPIE 8864, 886412 (2013).
[4] John Krist, "End-to-end numerical modeling of AFTA coronagraphs," Proc. SPIE 9143, 91430V (2014).
[5] Olivier Guyon, "Imaging Earth-like planets around late-type stars with low-inner working angle PIAA coronagraphy," Proc. SPIE 8864, 886414 (2013).

[6] A. Carlotti, N.J. Kasdin, and R. Vanderbei, “Shaped pupil coronagraphy with WFIRST-AFTA,” Proc. SPIE 8864, 886410 (2013).
[7] F. Shi, *et al*, "Low-order wavefront sensing and control (LOWFSC) for WFIRST/AFTA Coronagraph," American Astronomical Society 225th Meeting, (Seattle, Washington, 4-8 January 2015).
[8] F. Shi, , *et al* "Low-order wavefront sensing and control (LOWFSC) for WFIRST/AFTA Coronagraph," J. of Astronomical Telescopes, Instruments, and Systems, JATIS 15049, submitted (2015).
[9] E. Sidick, S. Shaklan, A. Give’on, and B. Kern, "Studies of the effects of actuator errors on the HCIT/PIAA contrast performance,” Proc. SPIE, 7731, 7731-4T (2010).
[10] J. Krist, B. Nemati, and B. Mennesson "Numerical modelling of the proposed WFIRST-AFTA coronagraphs and their predicted performances," J. of Astronomical Telescopes, Instruments, and Systems, JATIS 15049, submitted (2015).
[11] Trauger, J., Moody, D., Gordon, B., “The hybrid Lyot coronagraph for exoplanet imaging and spectroscopy with the WFIRST/AFTA and probe-class space missions,” Proc. SPIE, 9143 (2014).
[12] Amir Give’on *et al*, “Broadband wavefront correction algorithm for high-contrast imaging system,” Proc. SPIE 6691, 66910A (2007).
[13] E. Bloemof and J. Wallace, “Phase contrast techniques for wavefront sensing and calibration in adaptive optics,” Proc. SPIE. 5169, 309-320 (2003).